

Scattering Spectroscopy of Plasmonic Janus Particles

Felix H. Patzschke and *Frank Cichos

Abstract

Plasmonic Janus particles consist of dielectric core particles with a thin metallic cap on one side and are widely used in active matter research. [1] The plasmonic cap enhances optical scattering and absorption, allowing for self-propulsion through temperature gradients as well as efficient trapping and tracking. [2, 3] The asymmetry of such a particle gives rise to surface plasmon modes whose excitation is sensitive to the angle at which the particle is illuminated. Even though the angle of illumination strongly influences the particle's scattering response, the optical properties of such metallic caps have hardly been investigated.

We probe the light scattering of individual micrometre-sized, spherical, Au-coated Janus particles by means of Selective Illumination Multiplexed Fourier Plane Spectroscopy. This novel method allows us to explore microparticles' scattering characteristics resolved for wavelength, angle of illumination and scattering angle.

In addition, we supplement our experimental results with finite-element simulations and correlate spectral markers to orientation-dependent surface plasmon modes. This additional information on the correlation of angular and spectral information could pave the way for new methods of orientation detection. They also shed new light on the interaction of such spherically capped particles with light inducing forces and torques. [4, 5]

Introduction

Janus particles (JPs) with a plasmonically active cap are a widely-used tool in active matter research: Through the absorption of visible light, the cap can be heated efficiently. In conjunction with the anisotropy of the particle, this facilitates directed self-propulsion. Meanwhile, the enhanced optical scattering of the cap leads to good visibility in microscopy, particularly in the dark field, which, in turn, allows for accurate tracking of the motile particles.

[However, orientation studies are usually performed in 2D, as ...]

As widely applicable as these particles' light-matter interactions (LMIs) may be, they are certainly not trivial: The length scales of the surface curvature are in the same order of magnitude as the wavelengths of light in the interaction, such that approximations along the lines of ray optics or dipole scattering are invalid. In addition, the asymmetry of the particles leads to orientation-dependency of the LMI. These orientation-dependencies may manifest in counter-intuitive ways: Some purely numerical studies suggest that plasmonic JPs can stably rotate, powered by a linearly polarized light field. [4, 5]

As a first step towards an understanding of such effects, we study the scattered light from these JPs. We measure scattering spectra of individual JPs while varying the direction of illumination as well as resolving for the scattering angle. While orientation-dependent scattering studies of plasmonic nanostructures *have* been performed, [6] that has only been the case for Au nanostructures significantly smaller than the observation wavelengths. As such, no regard was given to the angular distribution of the scattered light. In our studies of micrometre-sized JPs in visible and NIR light

though, we find that the difference in shape of these distributions can lead to drastic, qualitative differences in measured scattering spectra.

We present an experimental method, which we use to study the LMI of plasmonic JPs consisting of a spherical polystyrene (PS) particle, 1 μm in diameter, with a 50 nm thick gold layer as the cap. We resolve the intensity of scattered light for wavelength and scattering angle. Though the theory of Mie [7] only makes predictions for maximally symmetric particles, it serves well as reference in the characterization of the LMI of plasmonic JPs.

We complement the measurement results with numerical simulations and find a good match between both methods' results. Through the analysis of the simulation results, we correlate peaks in the scattering spectra to orientation-dependent surface plasmon modes.

Methods

Experiments

Sample Preparation

The JPs consisted of spherical PS beads, coated with a layer of gold, 50 nm thick on average, on one side, with a 5 nm thick layer of chromium as a binding agent in between. A 30 μl droplet was placed on a cover slip and the JPs in solution were left to sediment for 10 minutes. Afterwards, the solvent was blown off using nitrogen gas, leaving the remaining JPs stuck on the coverslide. A second cover slip was placed on top, with a droplet of 1.5 μl of immersion oil¹ in between, such as to keep

¹Immersol 518 F, Carl Zeiss Jena GmbH

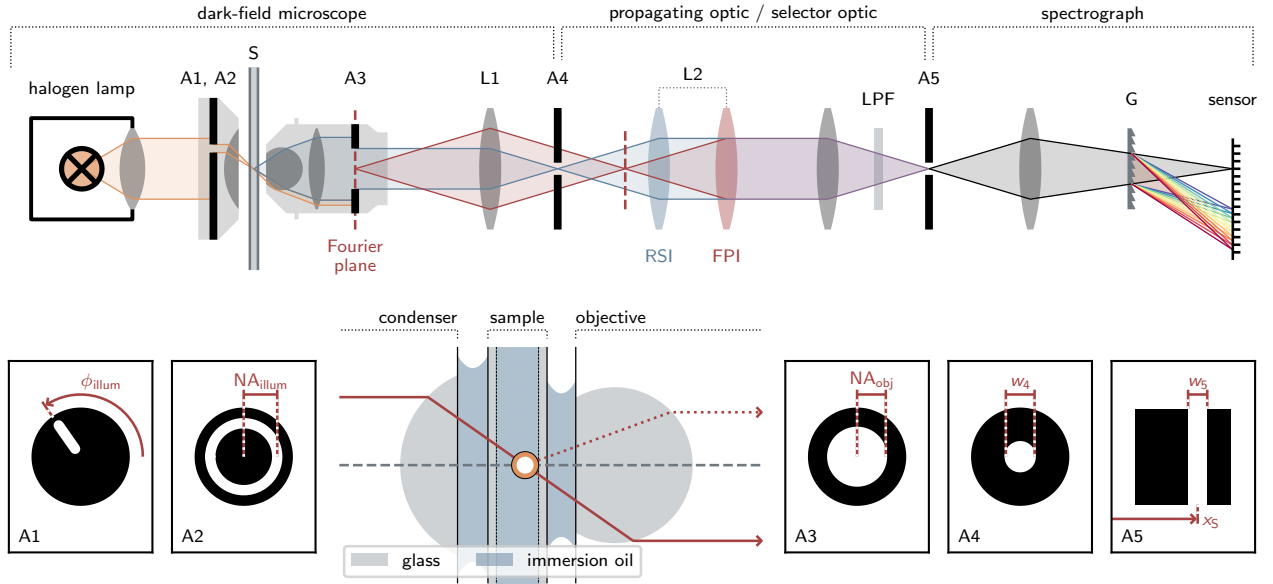


Figure 1: (top) Imaging light path. Schematics of the apertures (**A1-A5**) are shown below. A4 lies in an image plane, A1-A3 lay in Fourier planes. Depending on the placement of L2, either the image plane or the Fourier plane may be imaged onto A4, and subsequently the camera sensor. In the vicinity of the particle under observation (**bottom center**), the ambient refractive index is virtually homogenous, due to the usage of immersion oil inside the sample.

the ambient refractive index constant in the vicinity of the particles.

Optical Setup

The imaging setup is sketched in Figure 1C. Its basis was formed by a standard dark-field microscope, constructed around an OLYMPUS IX71 microscope base. A confocal aperture in the image plane of the dark-field microscope was used to isolate an individual particle. A homebuilt spectrograph was used to extract spectral information from the microscope image. The microscope and spectrograph sub-assemblies were linked by a simple propagating optic, with which either the image plane wherein the aperture lay or the back focal plane (BFP) of the microscope objective could be chosen to be projected onto the slit (A5).

The real-space-imaging mode was used to select particles for measurement as well as for spectral measurements in which the scattering angle was not resolved. The BFP-imaging mode was used to record spectrally resolved Fourier-space scattering maps of the JP under observation. To that end, the slit A5 was slowly translated across the BFP image while recording an image sequence, such that the camera would record one spectrally dispersed vertical line of the BFP image at a time. This step being the spatio-temporal multiplexing of the line-wise spectral signals, the corresponding de-multiplexing is done later, by appropriately re-arranging the intensity data from the image stack. [This procedure is described in detail in the supplementary material and in [8].] The accumulation time for one such dataset was approximately 15 minutes.

Measurements had to be corrected for the spectral response function of the setup. This was recorded

by opening the objective's back aperture (A3) fully, allowing the illumination light to pass through the entire assembly.

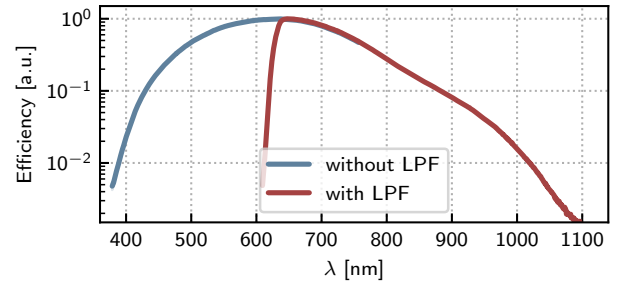


Figure 2: Spectral efficiency of the optical setup.

The spectral efficiency of the setup, being the accumulated product of the lamps's emission spectrum, the camera's quantum efficiency and the optics' transmittivities, is illustrated in Figure 2. We deem this sufficient for wavelengths between 400 nm and 1000 nm.

[I'm leaving out the laser for position calibration stuff. → supplement?]

Numerical Methods

Definition of the Orientation

In order to assure comparability between experimental and numerical results in terms of the orientation of the system, we define three unit vectors;

\hat{z} , the symmetry axis of the particle, oriented such that the Au cap lies in the positive and the PS side in the negative z -direction,

\hat{k}_0 , the propagation direction of the incident light, with respect to which scattering angles are defined and

\hat{o} , the "forward" direction along the optical axis, equivalent to the central axis of the objective's collection cone.

In terms of these, the *out-of-plane orientation* of the JP is defined as $\alpha := \angle(\hat{o}, \hat{z})$. Similarly, we define the *illumination angle* $\zeta := \angle(\hat{k}_0, \hat{z})$.

Scattering angles are defined for each plane-wave contribution to the scattered field: Let that contribution have a propagation direction \hat{k}' . Then, $\theta := \angle(\hat{k}', \hat{k})$ is the *polar component* of the *scattering angle*. Additionally, there is an azimuthal component ϕ , the choice of reference point for which being somewhat arbitrary. In the following, it will be chosen such that if \hat{k}' lies in the (\hat{k}, \hat{z}) plane, then $\phi = 0$.

These definitions are illustrated in Figure 3.

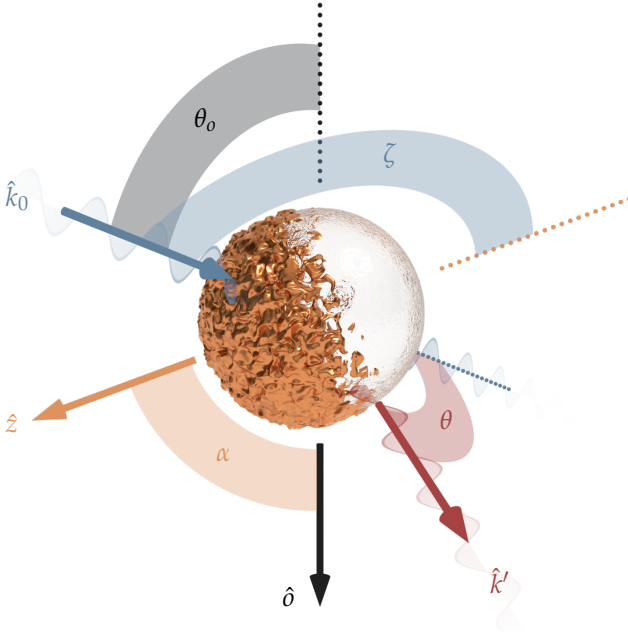


Figure 3: Unit vectors and angles defining the orientation of the system.

Finite-Element Simulation

The finite-element simulations were performed in COMSOL Multiphysics 6.1. [\[Reference that the COMSOL model is qualitatively the same as in \[5\].\]](#)

The model was set up as follows: A polystyrene (PS) sphere ($r = 0.5 \mu\text{m}$), centered at the origin, represents the core of the JP. The gold cap is modelled as half of an ellipsoidal shell around the PS sphere, cut off in the $z = 0$ plane. Its semi major axis is parallel to \hat{z} with a length of $0.55 \mu\text{m}$, its semi minor axes with length $0.51 \mu\text{m}$ lie in the (x, y) plane.² This gives a thickness of 50 nm at the apex and a width of 10 nm to the rim. [\[sketch?\]](#)

² $\hat{x}, \hat{y}, \hat{z}$ form a right-handed orthonormal basis of \mathbb{R}^3 .

For the complex refractive index of gold, the values by Johnson & Christy [9] were used. The medium surrounding the particle was modelled with a refractive index of 1.51 to mimic the immersion oil used in the experiments.

As parameters, the simulation takes in the illumination angle ζ and the incident (vacuum-)wavelength λ , such that

$$\vec{k}_0 = \frac{2\pi n}{\lambda} (\cos \zeta \cdot \hat{z} + \sin \zeta \cdot \hat{x})$$

is the wave vector of the incident light field.

From the numerical solution to Maxwell's field equations for each fixed parameter vector, the far-field intensities $d\mathcal{I} : S^2 \ni \Omega \mapsto d\mathcal{I}(\Omega)$ of the scattered field and the scattering cross-section σ_{sca} are calculated.

Selective Integration

In the experiment, scattered light can only contribute to recorded scattering signals if it is collected by the objective. While the "true" scattering intensity is the integral over the angular distribution of scattered light,

$$I_{\text{sca}}(\lambda) = \oint_{S^2} d\mathcal{I}(\lambda, \Omega),$$

the measured value corresponds to the integration over a certain angular range,

$$I_{\text{sca,measured}}(\lambda) = \iint_{\mathcal{D}} d\mathcal{I}(\lambda, \Omega),$$

where $\mathcal{D} \subseteq S^2$ is the set of propagation directions \hat{k}' , for which a plane wave component will pass through the objective aperture. Specifically, \mathcal{D} is the interior of a small circle which is centered around \hat{o} and whose angular radius ρ is defined by the numerical aperture of the objective,

$$\rho = \text{asin}\left(\frac{\text{NA}}{n_{\text{oil}}}\right),$$

according to the Abbe sine condition. [10, 11] [\[Sketch!\]](#) Analytically, this requirement can be formulated as

$$\mathcal{D} = \left\{ \hat{k}' \in S^2 \mid \angle(\hat{k}', \hat{o}) < \rho \right\}.$$

As the objective is not considered in the simulations of the scattering process per se, appropriate values for \hat{o} and NA have to be chosen now, in order to emulate an experiment: We first choose a fixed α and then compute a sampling of pairs $(\hat{k}'_0, \hat{o}') \in S^2|_{y=0} \times S^2$, such that

$$\angle(\hat{k}'_0, \hat{o}') = \theta_0 = \text{asin}\left(\frac{\text{NA}_{\text{DFC}}}{n_{\text{oil}}}\right),$$

the angle between the optical axis and the illumination cone from the dark-field condenser. We then choose the simulations corresponding to the illumination angles defined by \hat{k}'_0 and the fixed \hat{z} and integrate the simulated scattering intensities over the domains \mathcal{D}

defined by δ' and NA, accumulating the results over all pairs (\hat{k}'_0, δ') .

The end result of the selective integration is a sampled map

$$\alpha, \text{NA} \mapsto [\lambda \mapsto I_{\text{sca,measured}}],$$

i.e. a scattering spectrum $\lambda \mapsto I_{\text{sca,measured}}$ as measured for each sampled α , NA.

Results

Validation

In order to validate the experimental setup, the scattering spectra of 65 nm AuNPs were measured. We decided on the use of these much smaller particles because the expected resonance peak in the scattering spectrum would be as narrow as possible, giving a good indication as to the spectral resolution of the measurement. Furthermore, the shape of the angular distribution of scattered light would not change appreciably over the spectral range of interest, causing the measured and full scattering cross-sections to only differ by a constant factor. In Figure 4A, the measured scattering spectra are shown together with the prediction from Mie theory [7], computed using the values by Johnson & Christy [9] for the complex refractive index of gold.

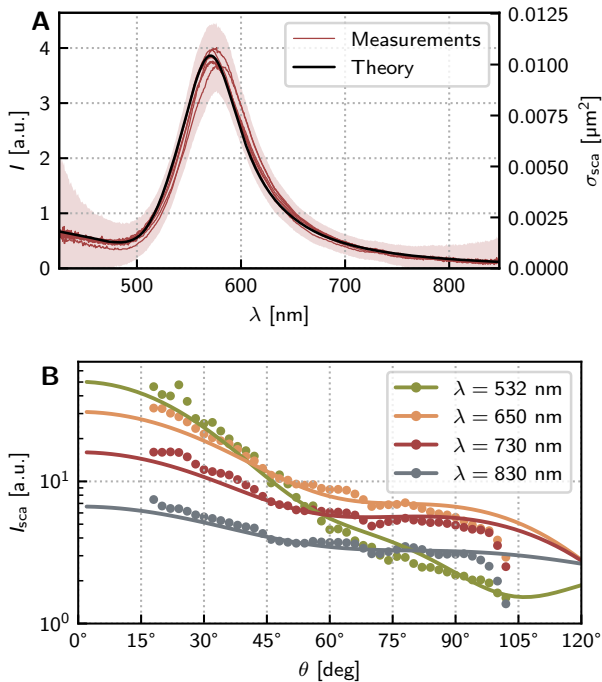


Figure 4: Validation measurements. **A:** Scattering spectrum of 65 nm Au NPs. The shaded area corresponds to the maximum noise in the measurements. **B:** Scattering intensity of a spherical Au NP ($d = 250$ nm) versus the scattering angle for various wavelengths. The lines show the predictions of GLMT [12], scaled by a constant factor to match the points showing the measurement results.

We find a good match between the measured and theoretical spectra. As the particles were significantly smaller than any wavelength considered, the scattered field is well-approximated by a dipole field. Still, the shift of the measured scattering peaks towards the red end of the spectrum, caused by the slightly flatter intensity distribution at longer incident wavelengths is significant.

To test the BFP spectroscopy, we chose larger Au particles ($d = 250$ nm), first and foremost for their much greater brightness in the dark field: In the BFP measurement, the scattered light is distributed over a larger area on the sensor, lowering the SNR. The greater scattering cross-section of larger particles remedies that issue. Nonetheless, the scattering cross-section of one such AuNP could be expected to be smaller than that of a JP as used later-on, implying that if the measurement was valid for the AuNPs, it would also be for the JPs. In addition, with a size close to the wavelengths under consideration, a perceptible change to the angular intensity distributions could be expected.

The results are shown and compared to the predictions of GLMT³[12, 13] in Figure 4B. Again, we find good agreement between experiment and theory.

Dark-Field Spectra

Recorded scattering spectra of the JPs are shown in Figure 5, along with numerical predictions. The results from both methods agree reasonably well, with the measured curves falling within a standard deviation of the average⁴ of the numerically obtained spectra for the most part.

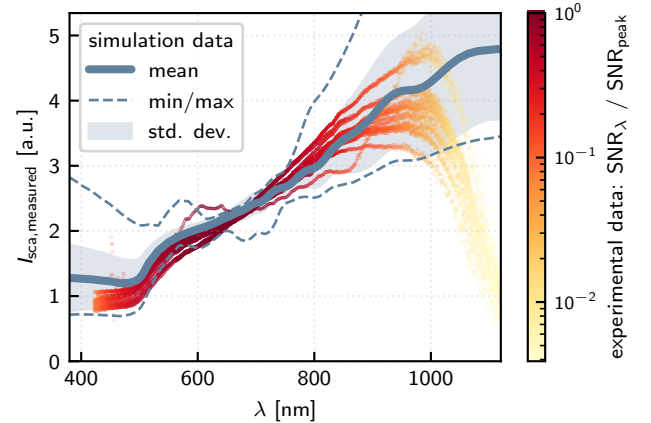


Figure 5: Measured scattering spectra (orange) atop value range as determined by simulation + emulation (blue).

All spectra show a sharp upward bend at 500 nm, the same as can be seen in the scattering spectra of similar-sized Au spheres. For longer incident wavelengths, we generally observe the scattering intensity to monotonously increase.

³Generalized Lorentz-Mie Theory

⁴[explain that average]

Between 900 and 1000 nm, the degraded efficiency of the measurement setup causes the relative influence of bleed light and sensor noise to increase, rendering the measurements increasingly unreliable.⁵ Hence, the measured spectra diverge from one another. The numerical results suggest that the trend of approximately linear increase should continue.

Consistent between all measurements, there is a bump at 550 nm. We attribute this to the LSPR of gold, though the otherwise increasing characteristic of the spectra diminishes the distinct peak that it would produce in the scattering spectra of small AuNPs into a mere bump.

Neither in the measured, nor in the numerically obtained spectra were we able to discern any obvious features that we could relate to an orientational parameter of the system.

Dark-Field Spectra under Selective Illumination

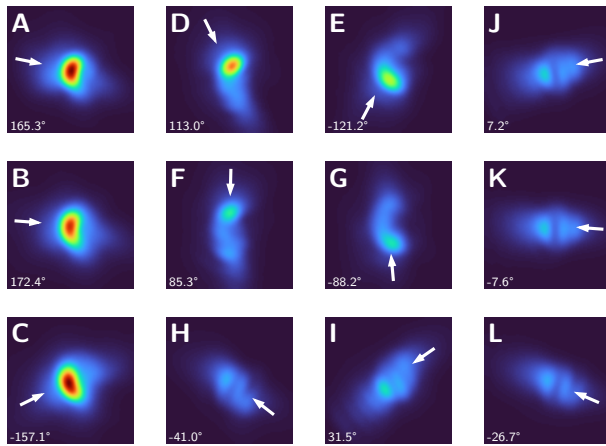


Figure 6: Dark-field images of a JP under selective illuminations. The respective in-plane angles are noted in the lower left corner.

[Particle appears much brighter when illuminated from the Au side. It stands to reason that its out-of-plane orientation made it such that when the aperture was rotated such that the PS side would be illuminated, the light *actually* hit side-on. (I.e. cap pointing ca. 30° up towards the condenser)]

With the selective illumination mode, we demonstrate the dependence of the JP's scattering intensity on the propagation direction of the incident light. [need to have another look at the data]

Scattering Spectra

Using the real-world optical setup, it is not possible to capture all of the scattered light. Yet, from the simulations, we can readily extract predicted values of the scattering cross-section of the JP: With the illumination

angle as a parameter, we obtain a family of scattering spectra:

$$\zeta \mapsto [\lambda \mapsto \sigma_{\text{sca}}],$$

each spectrum $\lambda \mapsto \sigma_{\text{sca}}$ corresponding to a specific illumination angle ζ . Figure 7 shows the scattering spectra for the maximally symmetric orientations of $\zeta = 0$ and $\zeta = \pi$, as well as for $\zeta = \pi/2$, i.e. the case wherein $\hat{k}_0 \perp \hat{z}$. A scattering intensity map, taking into account other sampled illumination angles is shown in [supplementary figure].⁶

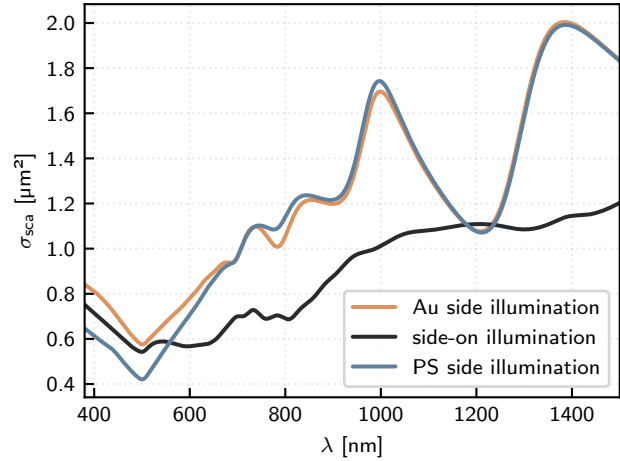


Figure 7: Simulated scattering spectrum of the JP under illumination from the Au side (yellow), from the PS side (blue) and from the equatorial side (black).

The scattering spectra differ significantly from the measured dark-field spectra, though some correspondences between features can be inferred: The previously noted increasing trend is, once again, present, as is the sharp upward bend at 500 nm. However, [distinct wobbles for $\lambda > 600$ nm, decrease of scattering cross-section up to the minimum at 500 nm]

Within the visible part of the spectral range, the increase of the scattering cross-section coincides with that of the measured intensities. In the NIR range, the measured brightness increases further; this is due to the broadening of the forward scattering peak.

For wavelengths beyond 700 nm, the scattering cross-sections, between illumination from the Au side and from the PS side, are virtually the same. They are, moreover, significantly larger than that for side-on illumination, on average. However, at $\lambda = 1210$ nm, they have a local minimum where the scattering cross-section is less than that for side-on illumination. This points at a polar plasmon mode that is being excited out-of-phase. [Explain better what I mean.] [Curiously, the peaks in the absorption spectra don't line up with either the valleys or the peaks in the scattering spectra. They don't for AuNPs either.]

⁵[I'm using the word "increase" too often, but I can't come up with anything else.]

⁶[leaving this out, not because the other spectra would be trivial combinations of the principal ones (they're not), but because a discussion of those would entail a decomposition into the underlying effects, which (a) would necessitate finding them in the high-symmetry cases first and (b) is outside the scope of this work.]

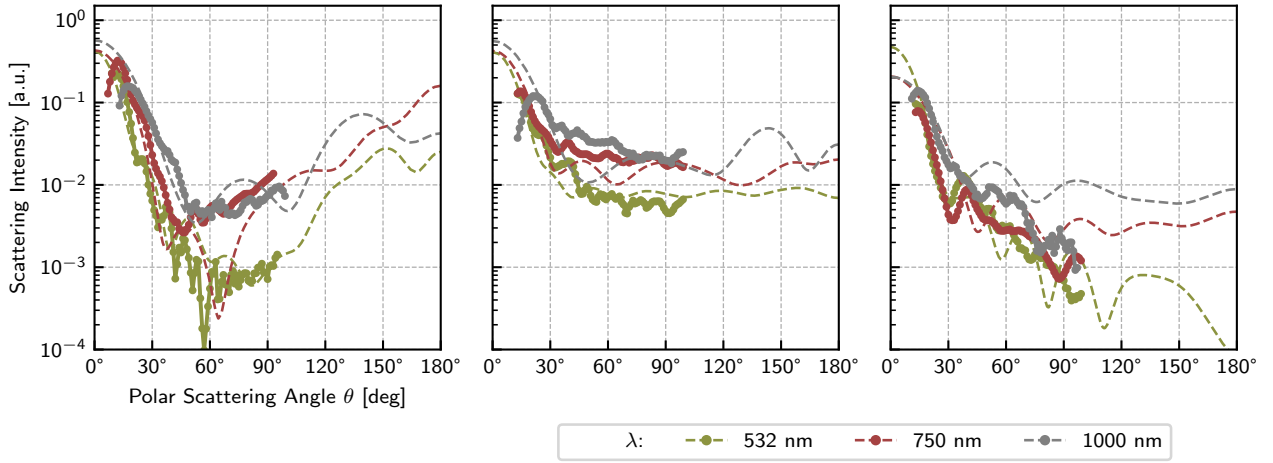


Figure 8: Scattering intensity of the JP versus scattering angle for various wavelengths. The points correspond to measured intensities while the lines are simulation results. **A:** PS side illumination. **B:** Au side illumination. **C:** side-on illumination.

This is due to only scattered light which is emitted in such a direction that it is collected by the objective contributing to the measured scattering intensity, while the simulated scattering spectra take into account the energy flow density of the scattered field itself.

Fourier Plane Spectra

In the multiplexed Fourier plane spectroscopy, the angular distributions of the scattering intensity became visible. We performed measurements under three different settings of the selective illumination, each chosen to match as closely as possible the cases of Au-side, PS-side and side-on illumination. Because the exact out-of-plane angle of the particle under observation is unknown and in order to allow for easier comparison of measured and numerical data, we extracted 1-dimensional intensity profiles along the polar coordinate from the Fourier plane images. Measured and simulated scattering profiles are shown in Figure 8.

For all illumination directions, most of the scattered light is only lightly deflected off of the propagation direction of the incident light. However, there were qualitative distinctions between the distributions that hold over the entire spectral range under consideration: The peak brightness was highest for illumination from the Au side, while a wider peak and significant side-ways scattering accumulated into a greater absolute brightness under illumination from the PS side.

The behaviours described also hold true for the full images.

Unsurprisingly, the distributions were symmetric about the axis of illumination. This was not the case for the side-on illumination, where light was preferentially scattered in the direction of the Au side.

The simulated far-field patterns show the same results.

Discussion

Spectra

[The average of]⁷ The thus computed spectra reproduce the measured dark-field spectra well. Meanwhile, details such as the local maxima of the full scattering spectra are lost. [with the possible exception of a small wobble at 850 nm, but it's unclear how exactly it arises. Maybe it's the $k = \pm 4$ -peak?]

[We find that the scattering cross-section heavily depends on the orientation of the JP.] Over the spectral range that we analyzed, though decidedly not in general, the scattering efficiency of the particle was ... greater if it was illuminated from either the Au or the PS side than if it was illuminated side-on. In both cases, the scattering spectra have multiple peaks. Between axial and side-on illumination, though, there is no clear correspondence between these peaks.

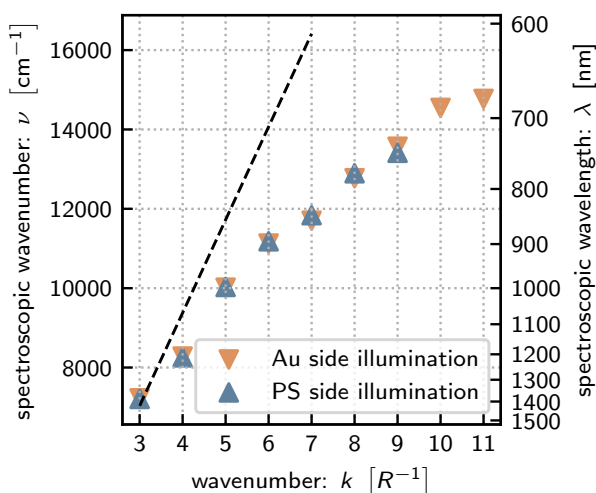
E.g., for side-on illumination, there is a scattering peak at $\lambda \approx 550$ nm, that has no counterpart in the spectra for axial illumination. We ascribe this peak to the nanostructure plasmon resonance of gold: It sits right around that wavelength and it is only under side-on illumination that the incident electric field may be perpendicular to the surface of the Au cap at its points of highest curvature, that being the cap's perimeter.

The bump at $\lambda \approx 550$ nm is discernable in both real and emulated measurements, while only appearing in the raw scattering cross-sections for side-on illumination. Notably, this peak occurs at the same wavelength as the main LSPR for an arbitrarily small AuNP. We reason that this plasmon is excited in the rim of the cap by electric fields that are perpendicular to the Au surface in its regions of maximal curvature.

Conversely, the peak at $\lambda \approx 996$ nm is present un-

⁷[most of the individual sample spectra fit reasonably well but there are some outliers. The average fits nicely, but ultimately one of those samples is likely the truth. And they have the same limitations in regards to details lost.]

der just the opposite circumstances, i.e. when $\hat{k} \parallel \hat{z}$. For these orientations, the system is rotationally symmetric in the polarization average and the surface plasmon propagates along the polar direction on the Au cap, inward for $\zeta = 0$ and outward for $\zeta = \pi$. A quantity akin to a wave vector can be assigned to the polar surface plasmon mode, by counting the sign changes of the surface charge density on a geodesic path from the apex of the cap to its rim. For the 996 nm peaks, this means $\tilde{k} = \pm 3$. [Similarly, we can assign such a pseudo wave vector to all the other peaks in the scattering spectra for axial illumination. The result is Figure 9.]



Neither of these peaks is present⁸ in the scattering spectrum of an equivalently sized Au sphere. This implies that [either] the associated surface plasmon modes do not exist on a closed sphere in this form [or the AuS spectrum is more closely related to the orientation-average of the JP spectra than it is to any single one of them].

The weak scattering of even-numbered resonances is due to the surface charge density having opposite signs in corresponding areas of the inside and outside of the gold cap. Whether the same effect could be observed on a core-shell particle of equivalent size is unclear: On one hand, it has been suggested that light interaction properties of JPs can be approximated as a mix between those of solid particles and of core-shells [Citation: black paint]. On the other hand, visual inspections of the time-dependent solutions for the electric field suggest that the surface charge densities on the in- and outside of the cap are coupled via the

boundary of the cap rather than through transmission through it. This would imply that the odd-even splitting would not happen on a CS particle, as transmission through the Au layer would be the only possible way of coupling the inside field to the outside one.

Comparing the angular distributions to those of a Mie particle though, there is clear similarity: Non-global maxima become more well-distinguished and fewer in number as wavelength increases. The same happens as the direction of illumination is changed from $\hat{k} \perp \hat{z}$ to $\hat{k} \parallel \hat{z}$: Both parameter changes can, from a Mie-theoretical point of view, be understood as a decreasing size parameter and thus the transition from the ray optics regime ($\lambda \ll R$) to a dipole model ($\lambda \gg R$).

[A summary figure of sim results: scattering spectra, Mie plots and the like]

Distributions

Conclusion & Outlook

[Results] We find that the anisotropy of the JP causes certain features to appear in and disappear from its scattering spectrum under certain orientations, particularly in the NIR range.

Coarse-grained simulations for longer wavelengths (up to 1400 nm) suggest that the drop-off that was originally inferred in [8] does not manifest in actuality.

Interesting things to do with this in the future might be...

- Direct analysis of the surface plasmons: Decomposition of the tangential electric field in an appropriate basis (vector hemispherical harmonics?) to find relative excitation of every (important) surface plasmon mode, depending on wavelength and illumination angle.
- Real-time spectroscopy to track a JP's out-of-plane angle.

[Further investigation of the angular distributions could help develop a computationally inexpensive theory of the pressure cross-section of JPs.]

References

1. Bregulla, A. P. & Cichos, F. Flow fields around pinned self-thermophoretic microswimmers under confinement. *J. Chem. Phys.* **151**, 044706. <https://doi.org/10.1063/1.5088131> (2019).
2. Auschra, S., Bregulla, A., Kroy, K. & Cichos, F. Thermotaxis of Janus Particles. *Eur. Phys. J. E* **44**. <https://doi.org/10.1140/epje/s10189-021-00090-1> (2021).
3. Selmke, M., Khadka, U., Bregulla, A. P., Cichos, F. & Yang, H. Theory for controlling individual self-propelled micro-swimmers by photon nudging I: directed transport. *Phys. Chem. Chem. Phys.* **20**, 10502. <https://doi.org/10.1039/c7cp06559k> (2018).
4. Ilic, O. *et al.* Topologically enabled optical nanomotors. *Sci. Adv.* **3**, e1602738. <https://advances.sciencemag.org/content/3/6/e1602738> (2017).
5. Patzschke, F. H. *Finite Elements Simulations of Optical Torques on Metal-Dielectric Janus Particles* Bachelor's Thesis (Universität Leipzig, 2020).
6. Islam, M. M., Hossen, M. M., Koschny, T. & Hillier, A. C. Shape- and Orientation-Dependent Scattering of Isolated Gold Nanostructures Using Polarized Dark-Field Microscopy. *J. Phys. Chem. C* **125**, 11478–11488. eprint: <https://doi.org/10.1021/acs.jpcc.1c03671>. <https://doi.org/10.1021/acs.jpcc.1c03671> (2021).
7. Mie, G. Beiträge zur Optik trüber Medien, speziell kolloidaler Metallösungen. *Annalen der Physik* **330**, 377–445. <https://doi.org/10.1002/andp.19083300302> (3 1908).
8. Patzschke, F. H. *Orientation-dependent Spectroscopy of Plasmonic Janus Particles* Master's Thesis (Universität Leipzig, 2023).
9. Johnson, P. B. & Christy, R. W. Optical Constants of the Noble Metals. *Phys. Rev. B* **6**, 4370. <https://doi.org/10.1103/PhysRevB.6.4370> (1972).
10. Wagner, R., Heerklotz, L., Kortenbruck, N. & Cichos, F. Back focal plane imaging spectroscopy of photonic crystals. *Appl. Phys. Lett.* **101**, 081904. <https://doi.org/10.1063/1.4746251> (2012).
11. Wagner, R. & Cichos, F. Fast measurement of photonic stop bands by back focal plane imaging. *Phys. Rev. B* **87**, 165438. <https://doi.org/10.1103/PhysRevB.87.165438> (2013).
12. Gouesbet, G. & Gréhan, G. *Generalized Lorenz–Mie Theories* Second Edition. ISBN: 978-3-319-46873-0 (Springer, Heidelberg, 2017).
13. Bohren, C. F. & Huffman, D. R. *Absorption and Scattering of Light by Small Particles* Wiley Professional Paperback Edition, 82–129, 136. ISBN: 978-0-471-29340-8 (John Wiley & Sons, Weinheim, 1998).

Acknowledgements

[...]

Author Contributions

F.C. and F.H.P. designed the experiments; F.H.P. constructed the optical setup, performed the experiments, implemented the simulations and conducted the data analysis; F.H.P. wrote the manuscript; All authors reviewed the manuscript.

Competing Interests

The authors have no competing interests to declare.

Additional Information

[...]